

Article

Multi-Field Coupling Dynamics Modeling of Aerostatic Spindle

Guoda Chen ^{1,2,3,*}  and Yijie Chen ^{2,3}¹ State Key Laboratory of Fluid Power and Mechatronic Systems, Zhejiang University, Hangzhou 310027, China² College of Mechanical Engineering, Zhejiang University of Technology, Hangzhou 310023, China; chenyj@zjut.edu.cn³ Key Laboratory of Special Purpose Equipment and Advanced Processing Technology, Ministry of Education and Zhejiang Province, Zhejiang University of Technology, Hangzhou 310023, China

* Correspondence: gchen@zjut.edu.cn

Abstract: The aerostatic spindle in the ultra-precision machine tool shows the complex multi-field coupling dynamics behavior under working condition. The numerical investigation helps to better understand the dynamic characteristics of the aerostatic spindle and improve its structure and performance with low cost. A multi-field coupling 5-DOF dynamics model for the aerostatic spindle is proposed in this paper, which considers the interaction between the air film, spindle shaft and the motor. The restoring force method is employed to deal with the times varying air film force, the transient Reynolds equation of the aerostatic journal bearing and the aerostatic thrust bearing is solved using ADI method and Thomas method. The transient air film pressure of aerostatic bearings is obtained which clearly presents the influence induced by the tilt motion of the spindle shaft. The motion trajectory of the spindle shaft is obtained which shows different stability of the shaft under different external forces. The dynamics model shows good performance on simulating the multi-field coupling behavior of the aerostatic spindle under external force. which is quite meaningful and useful for the further research on the dynamic characteristics of the aerostatic spindle.

Keywords: dynamics modeling; aerostatic spindle; rotor trajectory; stability; Reynolds equation



Citation: Chen, G.; Chen, Y. Multi-Field Coupling Dynamics Modeling of Aerostatic Spindle. *Micromachines* **2021**, *12*, 251. <https://doi.org/10.3390/mi12030251>

Academic Editors: Benny C. F. Cheung and Jiang Guo

Received: 10 February 2021
Accepted: 25 February 2021
Published: 1 March 2021

Publisher's Note: MDPI stays neutral with regard to jurisdictional claims in published maps and institutional affiliations.



Copyright: © 2021 by the authors. Licensee MDPI, Basel, Switzerland. This article is an open access article distributed under the terms and conditions of the Creative Commons Attribution (CC BY) license (<https://creativecommons.org/licenses/by/4.0/>).

1. Introduction

The aerostatic spindle plays a key role in an ultra-precision machine tool in the nano-precision machining, which directly affects the machining quality [1,2]. Generally, the shaft of the aerostatic spindle is directly driven by a permanent magnet synchronous motor (PMSM) and supported by the aerostatic bearing, including the journal bearing and the thrust bearing [3].

Compared to the aerodynamic bearing, the aerostatic bearing provides higher capacity and steady force, while it contains more complex mechanism contributes to the dynamic behavior of aerostatic spindle. During the operation of the aerostatic spindle, it shows the multi-physics field coupling characteristics, in which the coupling effect of air bearing, the shaft and the motor should be considered for fully understanding its dynamics behavior [4]. However, the previous literatures commonly focused on single factor or two factors while investigating the dynamic characteristics of the aerostatic spindle [5–8]. It has been pointed out that the existence of unbalanced magnetic force (UMF) caused by rotor eccentricity at the motor can have a considerable impact on the machined surface [9–11], thus, the electromagnetic factor is not negligible in the dynamics model of aerostatic spindle.

Rotor dynamics modeling is the preferred method to study the dynamic characteristics of a rotor-bearing system, by which we can get detailed information of how the rotor acts under different condition. Among the previous literature, the rotor dynamics modeling method was widely used for modeling the aerodynamic bearing-rotor system with 2-DOF (Degree of Freedom) [12–16], the rotor trajectory and the stability problem were analyzed.

Since performance superiority of aerostatic spindle emerges in recent years, the analysis on aerostatic spindle came out frequently and have made great progress. Wang [17] implemented the rotor dynamic model of aerostatic bearing-rotor systems which applied a spherical aerostatic bearing, and the nonlinear dynamic behavior of the rotor bearing system is analyzed. Similar works were done by Zhang et al. [18], they proposed forecast orbit method to deal with the transient gas lubricated Reynold equation, and the 2D rotor trajectory under different rotor speed and imbalance mass was obtained. Two-dimensional analysis can reflect the characteristics of aerostatic bearing to some extent but not as precise as the result of the 5-DOF model. In a 5-DOF model, the tilt motion, the displacement in axial direction and the conical movement of the shaft can be acquired while the 2-DOF model cannot, and these forms of movement are also proved to have significant influence on the machined surface quality by Zhang et al. [19]. To achieve this, Li et al. [20,21] presented the 5-DOF model of an aerostatic spindle in a fly-cutting machine, in which the air pressure distribution of journal bearing and thrust bearing was calculated and the displacement of the shaft in different directions was obtained. Xu and Jiang [22,23] analyzed the 5-DOF rotor dynamics model of an aerostatic spindle, in which the stability, the unbalance response, and the forced response of the rotor-bearing system were investigated. Both Li and Xu adopted the dynamic coefficient method in their model, however it may lose the numerical accuracy when taking this method which indeed largely improved the efficiency. By contrast, the restoring force commonly used in 2-DOF models aims to obtain force directly by solving the transient Reynold equation [24,25], and it can also obtain the torque in a 5-DOF model. It can be optimized of the dynamic coefficient method, but if this measure is taken, massive extra work needs to be done. Besides, the available research on aerostatic spindle modeling fail to consider the electromagnetic factor, which has important effect on the motion error of the spindle.

In this paper, the electromagnetic factor is considered in the modeling of the aerostatic spindle, and the restoring force method is adopted. The finite difference method is adopted to discrete the transient Reynolds equation. The simulation for the motion trajectory of the spindle shaft is realized under the coupling of the restoring force of the aerostatic bearing, the UMF of PMSM and the external force on the shaft, where the shaft is regarded as a rigid rotor.

2. Mathematical Modeling of Aerostatic Spindle

The typical structure diagram of the aerostatic spindle is shown in Figure 1, the spindle shaft is directly driven by the motor, and the shaft is supported by an aerostatic journal bearing and two aerostatic thrust bearing.

Effectively modeling the dynamic behavior of the air film is quite necessary for the systematic and consistent air bearing design [26,27], thus, the modeling of the air film is of primary importance. The pressure distribution of the aerostatic bearing air film can be described by the Reynolds equation, and the Reynolds equation is obtained based on the Navier-Stokes Equations with following assumptions, the flow is isothermal, the gas viscosity is assumed to be constant, the pressure distribution in the vertical direction to the air film is assumed to be constant, the viscosity force is assumed to be much larger than inertia force, there is no velocity slip at the boundary, and the air is the ideal gas.

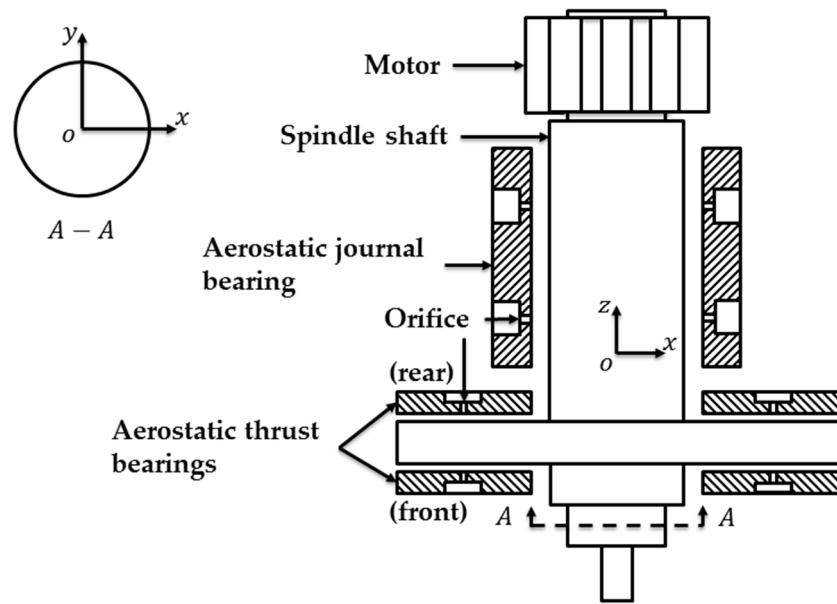


Figure 1. The structure diagram of the aerostatic spindle.

2.1. Modeling of Aerostatic Journal Bearing

The transient pressure distribution of aerostatic journal bearing can be modeled by the transient Reynolds equation in the Cartesian coordinate [28].

$$\frac{\partial}{\partial x} \left(\rho h^3 \frac{\partial p}{\partial x} \right) + \frac{\partial}{\partial z} \left(\rho h^3 \frac{\partial p}{\partial z} \right) + \frac{12\mu P_a}{\rho_a} \rho \tilde{v} \delta_k = 6\mu U_0 \frac{\partial(\rho h)}{\partial x} + 12\mu \frac{\partial(\rho h)}{\partial t} \quad (1)$$

where x is the circumferential coordinates of journal bearing, z is the axial coordinate of journal bearing, h is the air film thickness, p is the air film pressure, μ is the dynamic viscosity of the air, U_0 is the surface velocity of the shaft, \tilde{v} is the flow velocity of the supply air at the orifice, t represents the time, ρ is the air density, P_a and ρ_a are the pressure and density of the ambient air, $\delta_k = 1$ at the orifice and $\delta_k = 0$ at other position.

The dimensionless transient Reynolds equation is given by

$$\frac{\partial}{\partial \theta} \left(H^3 \frac{\partial P^2}{\partial \theta} \right) + \frac{\partial}{\partial Z} \left(H^3 \frac{\partial P^2}{\partial Z} \right) + Q \delta_k = \Lambda_J \frac{\partial(PH)}{\partial \theta} + 2\Lambda_J \frac{\partial(PH)}{\partial \tau} \quad (2)$$

The dimensionless parameters are defined as follows.

$$P = \frac{p}{P_s}, H = \frac{h}{C_r}, \theta = \frac{x}{L_j}, Z = \frac{z}{L_j}, Q = \frac{24\mu R^2 P_a}{C_r^3 P_s^2 \rho_a} \rho \tilde{v}, \tau = \omega t, \Lambda_J = \frac{12\mu \omega R L_j}{P_s C_r^2}$$

where L_j is the characteristic length of journal bearing, R is the radius of the journal bearing, C_r is the radial clearance between the journal bearing and the shaft, P_s is the supply pressure, Λ_J is the bearing number of the journal bearing, ω is the rotating speed of the shaft.

When the eccentricity or the tilt of the shaft happens as depicted in Figure 2, the thickness of the air film changes simultaneously, and the distribution of the air film thickness in the journal bearing can be expressed as

$$\begin{cases} h_{(i,j)} = C_r \cdot \left(1 + \varepsilon_{(i)} \cdot \cos\left(\theta_{(i,j)} - \alpha_{(i)}\right) \right) \\ H_{(i,j)} = 1 + \varepsilon_{(i)} \cdot \cos\left(\theta_{(i,j)} - \alpha_{(i)}\right) \end{cases} \quad (3)$$

$$\varepsilon_{(i)} = \varepsilon_{ib} + \frac{\sin(\beta) \cdot (i - i_b) \cdot L_s}{M_s} \tag{4}$$

$$\varepsilon_{ib} = \sqrt{(e_{ibx})^2 + (e_{iby})^2} \tag{5}$$

$$\alpha_{(i)} = \begin{cases} \arctg \frac{e_{iy}}{e_{ix}} & e_{ix} \geq 0 \\ \arctg \frac{e_{iy}}{e_{ix}} + \pi & e_{ix} < 0 \end{cases} \tag{6}$$

where $\varepsilon_{(i)}$ is the eccentricity at the node i , $\theta_{(i,j)}$ is the angle of air film at node i and j , $\alpha_{(i)}$ is the eccentric angle at the node i , i_b is the node of the barycenter, L_s is the axial length of the shaft, M_s is the number of nodes that L_s divided into, ε_{ib} is the eccentricity at the node i_b , β is the tilt angle of the shaft, e_{ibx} and e_{iby} are the eccentricity of the node i_b in x direction and y direction respectively, e_{ix} and e_{iy} are the eccentricity of the node i in x direction and y direction respectively.

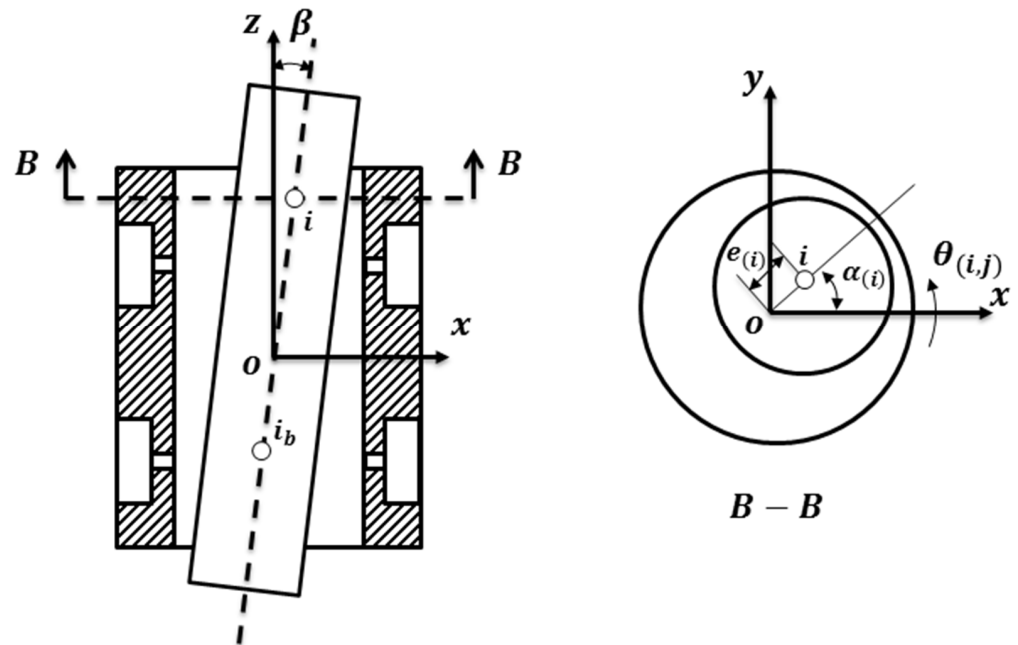


Figure 2. The tilt and the eccentricity of the shaft at the journal bearing.

The mass flow rate can be acquired based on the isothermal assumption given by Powell [29].

$$\dot{m} = \phi P_s A_{inlet} \sqrt{\frac{2\rho_a}{p_a}} \Psi \tag{7}$$

$$\Psi = \begin{cases} \left[\frac{k}{k-1} \left(\beta_i^{\frac{2}{k}} - \beta_i^{\frac{k+1}{k}} \right) \right]^{\frac{1}{2}} & \beta_i > \beta_k \\ \left[\frac{k}{2} \left(\frac{2}{k+1} \right)^{\frac{k+1}{k-1}} \right]^{\frac{1}{2}} & \beta_i \leq \beta_k \end{cases} \tag{8}$$

$$A_{inlet} = \begin{cases} \pi d C_r & \frac{d}{4} > C_r \\ \frac{\pi d^2}{4} & \frac{d}{4} \leq C_r \end{cases} \tag{9}$$

where ϕ is the coefficient of the mass flow rate, A_{inlet} is the minimum area of the flow channel, d is the diameter of the orifice, $\beta_i = p/P_s$ and $\beta_k = (2/(k+1))^{k/(k-1)}$.

As shown in Figure 3, the computational domain of the journal bearing film is meshed into $\theta(0 : N_j)$ and $Z(0 : M_j)$, the Periodic boundary condition, the Atmospheric boundary condition and the Mass flow boundary condition are also defined.

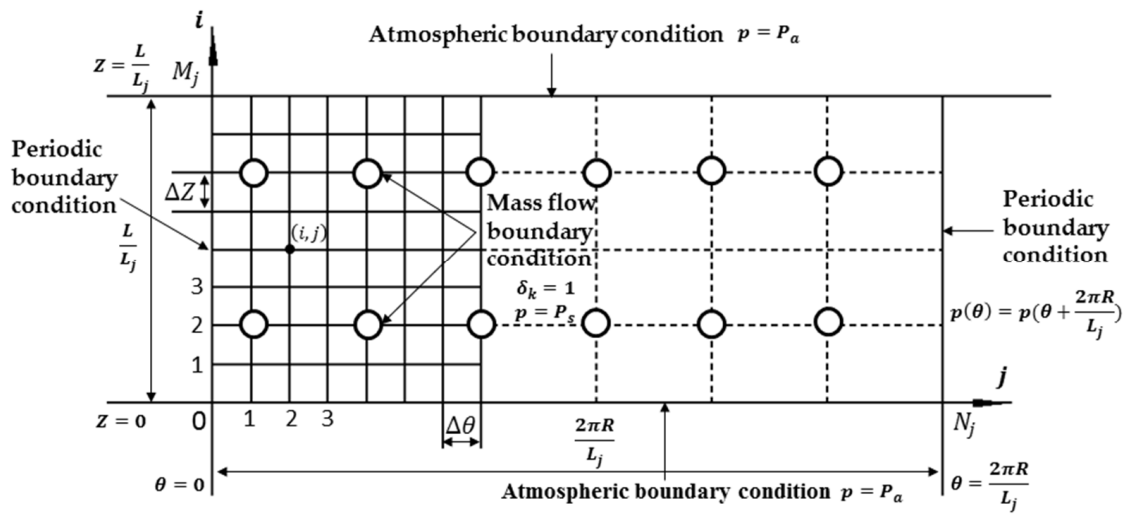


Figure 3. The computational domain of the journal bearing.

Submitting the expression $S = P^2$, the central difference method is adopted to discrete the variable in the θ and Z directions. The ADI method [18] is employed to simplify the implicit equation obtained after the discretization. The ADI format of the equation can be expressed as follows,

$$A_{(i,j)} S_{(i-1,j)}^{n+1} + B_{(i,j)} S_{(i,j)}^{n+1} + C_{(i,j)} S_{(i+1,j)}^{n+1} = D_{(i,j)} \tag{10}$$

$$A_{(i,j)} = -\frac{(H_{(i,j)}^n)^3}{(\Delta Z)^2} + 3(H_{(i,j)}^n)^2 \frac{H_{(i+1,j)}^n - H_{(i-1,j)}^n}{(2\Delta Z)^2} \tag{11}$$

$$B_{(i,j)} = \frac{2(H_{(i,j)}^n)^3}{(\Delta Z)^2} + \frac{\Lambda_J H_{(i,j)}^n}{P_{(i,j)}^n \Delta \tau} \tag{12}$$

$$C_{(i,j)} = -\frac{(H_{(i,j)}^n)^3}{(\Delta Z)^2} - 3(H_{(i,j)}^n)^2 \frac{H_{(i+1,j)}^n - H_{(i-1,j)}^n}{(2\Delta Z)^2} \tag{13}$$

$$D_{(i,j)} = Q\delta_k + 3(H_{(i,j)}^n)^2 \frac{(H_{(i,j+1)}^n - H_{(i,j-1)}^n)(S_{(i,j+1)}^n - S_{(i,j-1)}^n)}{(2\Delta\theta)^2} + (H_{(i,j)}^n)^3 \frac{(S_{(i,j+1)}^n - 2S_{(i,j)}^n + S_{(i,j-1)}^n)}{(\Delta\theta)^2} - \frac{\Lambda_J H_{(i,j)}^n (S_{(i,j+1)}^n - S_{(i,j-1)}^n)}{2P_{(i,j)}^n \Delta\theta} - \Lambda_J P_{(i,j)}^n \frac{(H_{(i,j+1)}^n - H_{(i,j-1)}^n)}{2\Delta\theta} + \frac{\Lambda_J H_{(i,j)}^n S_{(i,j)}^n}{P_{(i,j)}^n \Delta\tau} - 2\Lambda_J P_{(i,j)}^n \frac{(H_{(i,j+1)}^{n+1} - H_{(i,j-1)}^n)}{\Delta\tau} \tag{14}$$

$$E_{(i,j)} S_{(i,j-1)}^{n+2} + F_{(i,j)} S_{(i,j)}^{n+2} + G_{(i,j)} S_{(i,j+1)}^{n+2} = I_{(i,j)} \tag{15}$$

$$E_{(i,j)} = -\frac{(H_{(i,j)}^{n+1})^3}{(\Delta\theta)^2} - \frac{\Lambda_J H_{(i,j)}^{n+1}}{4P_{(i,j)}^{n+1} \Delta\theta} + 3(H_{(i,j)}^{n+1})^2 \frac{H_{(i,j+1)}^{n+1} - H_{(i,j-1)}^{n+1}}{(2\Delta\theta)^2} \tag{16}$$

$$F_{(i,j)} = \frac{2(H_{(i,j)}^{n+1})^3}{(\Delta\theta)^2} + \frac{\Lambda_J H_{(i,j)}^{n+1}}{P_{(i,j)}^{n+1} \Delta\tau} \tag{17}$$

$$G_{(i,j)} = -\frac{(H_{(i,j)}^{n+1})^3}{(\Delta\theta)^2} + \frac{\Lambda_J H_{(i,j)}^{n+1}}{4P_{(i,j)}^{n+1} \Delta\theta} - 3(H_{(i,j)}^{n+1})^2 \frac{H_{(i,j+1)}^{n+1} - H_{(i,j-1)}^{n+1}}{(2\Delta\theta)^2} \tag{18}$$

$$\begin{aligned}
 I_{(i,j)} = & Q\delta_k + 3\left(H_{(i,j)}^{n+1}\right)^2 \frac{\left(H_{(i,j+1)}^{n+1} - H_{(i,j-1)}^{n+1}\right)\left(S_{(i,j+1)}^{n+1} - S_{(i,j-1)}^{n+1}\right)}{(2\Delta Z)^2} + \\
 & \left(H_{(i,j)}^{n+1}\right)^3 \frac{\left(S_{(i+1,j)}^{n+1} - 2S_{(i,j)}^{n+1} + S_{(i-1,j)}^{n+1}\right)}{(\Delta Z)^2} - \Lambda_J P_{(i,j)}^{n+1} \frac{H_{(i,j+1)}^{n+1} - H_{(i,j-1)}^{n+1}}{2\Delta\theta} - \\
 & 2\Lambda_J P_{(i,j)}^{n+1} \frac{H_{(i,j)}^{n+2} - H_{(i,j)}^{n+1}}{\Delta\tau} + \frac{\Lambda_J H_{(i,j)}^{n+1} S_{(i,j)}^{n+1}}{P_{(i,j)}^{n+1} \Delta\tau}
 \end{aligned} \tag{19}$$

The increment in the marching direction Z is carried out at the time step of n + 1, and the increment in the marching direction θ is carried out at the time step of n + 2. The Equation (10) and Equation (15) can be solved by the Thomas method, Then, the pressure distribution of the aerostatic journal bearing is obtained. Base on the load formulas given by Rowe [30], the air film force (i.e., the restoring force of the journal bearing) of the journal bearing in x and y direction is given by

$$f_{bjx} = P_s L_j^2 \int_0^{\frac{L}{L_j}} \int_0^{\frac{2\pi R}{L_j}} P(Z, \theta, \tau) \cos(\alpha_{(i)}) d\theta dZ \tag{20}$$

$$f_{bjy} = P_s L_j^2 \int_0^{\frac{L}{L_j}} \int_0^{\frac{2\pi R}{L_j}} P(Z, \theta, \tau) \sin(\alpha_{(i)}) d\theta dZ \tag{21}$$

And the torque of the air film force (i.e., the restoring torque of the journal bearing) on the barycenter of the spindle shaft respect to the x axis and y axis is given by

$$t_{bjx} = P_s L_j^2 L_s \frac{i - i_d}{M_s} \int_0^{\frac{L}{L_j}} \int_0^{\frac{2\pi R}{L_j}} P(Z, \theta, \tau) \sin(\alpha_{(i)}) d\theta dZ \tag{22}$$

$$t_{bjy} = P_s L_j^2 L_s \frac{i - i_d}{M_s} \int_0^{\frac{L}{L_j}} \int_0^{\frac{2\pi R}{L_j}} P(Z, \theta, \tau) \cos(\alpha_{(i)}) d\theta dZ \tag{23}$$

2.2. Modeling of Aerostatic Thrust Bearing

The transient pressure distribution of aerostatic thrust bearing can be modeled by the transient Reynolds equation in cylindrical coordinate.

$$\frac{1}{r} \frac{\partial}{\partial r} \left(r p h^3 \frac{\partial p}{\partial r} \right) + \frac{1}{r^2} \frac{\partial}{\partial \theta} \left(p h^3 \frac{\partial p}{\partial \theta} \right) + \frac{12\mu P_a}{\rho_a} \rho \tilde{v} \delta_k = \frac{6}{r} \frac{\partial}{\partial \theta} (p h V_0) + 12\mu \frac{\partial (p h)}{\partial t} \tag{24}$$

where θ is the circumferential coordinates of journal bearing, r is the radial coordinate of journal bearing, V₀ is the surface velocity of the shaft.

The dimensionless transient Reynolds equation is given by

$$\frac{\partial}{\partial \theta} \left(H^3 \frac{\partial P^2}{\partial \theta} \right) + R_r \frac{\partial}{\partial R_r} \left(R_r H^3 \frac{\partial P^2}{\partial R_r} \right) + Q\delta_k = \Lambda_T \frac{\partial (PH)}{\partial \theta} + 2\Lambda_T \frac{\partial (PH)}{\partial \tau} \tag{25}$$

The dimensionless parameters are defined as follows.

$$P = \frac{p}{P_s}, H = \frac{h}{C_r}, R_r = \frac{r}{L_t}, Q = \frac{24\mu r^2 P_a}{C_r^3 P_s^2 \rho_a} \rho \tilde{v}, \tau = \omega t, \Lambda_T = \frac{12\mu \omega r^2}{P_s C_r^2}$$

where L_t is the characteristic length of journal bearing, and Λ_T is the bearing number of the thrust bearing.

The tilt motion of the shaft is considered to have influence on the air film thickness of the thrust bearing while the influence of the eccentricity is neglected. The tilt motion at the thrust bearing is shown in Figure 4, and the distribution of the air film thickness at the thrust bearing can be expressed as

$$h_{(i,j)} = C_r - \sin(\beta) \sin\left(\theta_{(i,j)} - \gamma_{(i)} + \frac{\pi}{2}\right) \cdot \left(\frac{i}{M_t}(R_b - R_a) + R_a\right) + \Delta z \quad (26)$$

where $\theta_{(i,j)}$ is the angle of air film at node i and j , $\gamma_{(i)}$ is the angle between the tile direction and the positive direction of x at the node i , i is the node number along the radial direction, R_a is the inner diameter of the thrust bearing, R_b is the out diameter of the thrust bearing, M_t is the number of thrust bearing nodes along the radial direction, Δz is the shaft displacement in the axial direction.

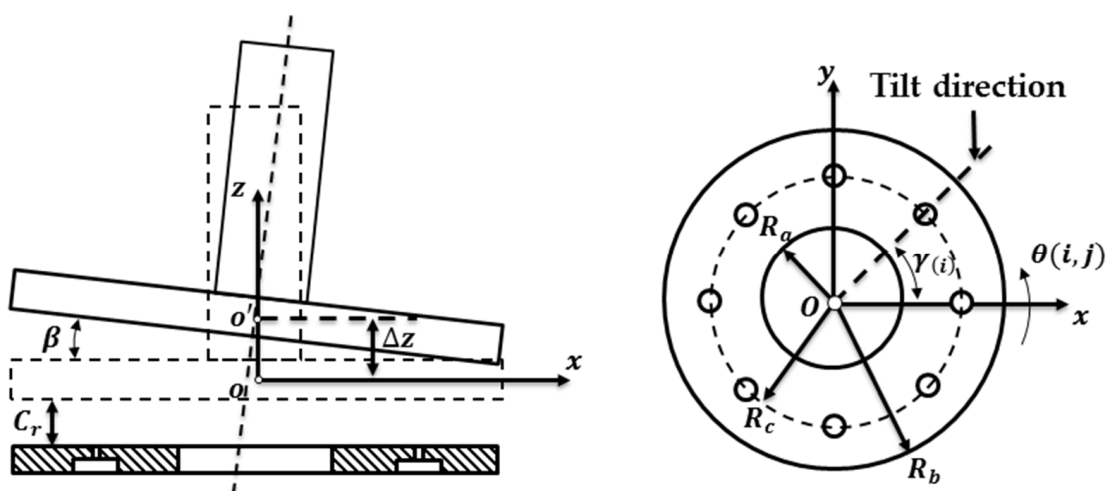


Figure 4. The tilt of the shaft at the thrust bearing.

As shown in Figure 5, the computational domain of the thrust bearing film is meshed into $\theta(0 : N_t)$ and $R_r(0 : M_t)$, the Periodic boundary condition, the Atmospheric boundary condition and the Mass flow boundary condition are also defined.

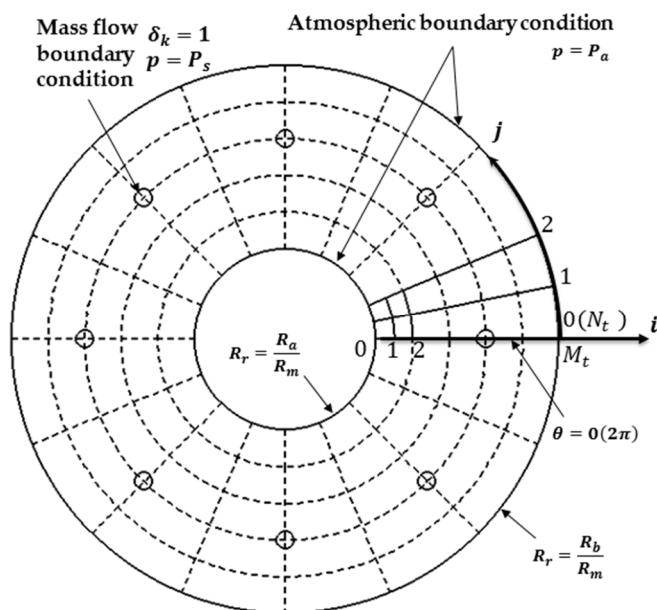


Figure 5. The computational domain of the thrust bearing.

Adopt the same treatment as the journal bearing, the ADI format of the equation obtained from thrust bearing can be expressed as

$$A_{(i,j)} S_{(i-1,j)}^{n+1} + B_{(i,j)} S_{(i,j)}^{n+1} + C_{(i,j)} S_{(i+1,j)}^{n+1} = D_{(i,j)} \tag{27}$$

$$A_{(i,j)} = -\frac{R_r^2 (H_{(i,j)}^n)^3}{(\Delta R_r)^2} + R_r^2 3(H_{(i,j)}^n)^2 \frac{H_{(i+1,j)}^n - H_{(i-1,j)}^n}{(2\Delta R_r)^2} + \frac{R_r (H_{(i,j)}^n)^3}{2\Delta R_r} \tag{28}$$

$$B_{(i,j)} = \frac{2R_r^2 (H_{(i,j)}^n)^3}{(\Delta R_r)^2} + \frac{\Lambda_T H_{(i,j)}^n}{P_{(i,j)}^n \Delta \tau} \tag{29}$$

$$C_{(i,j)} = -\frac{R_r^2 (H_{(i,j)}^n)^3}{(\Delta R_r)^2} - R_r^2 3(H_{(i,j)}^n)^2 \frac{H_{(i+1,j)}^n - H_{(i-1,j)}^n}{(2\Delta R_r)^2} - \frac{R_r (H_{(i,j)}^n)^3}{2\Delta R_r} \tag{30}$$

$$D_{(i,j)} = Q\delta_k + 3(H_{(i,j)}^n)^2 \frac{(H_{(i,j+1)}^n - H_{(i,j-1)}^n)(S_{(i,j+1)}^n - S_{(i,j-1)}^n)}{(2\Delta\theta)^2} + (H_{(i,j)}^n)^3 \frac{(S_{(i,j+1)}^n - 2S_{(i,j)}^n + S_{(i,j-1)}^n)}{(\Delta\theta)^2} - \frac{\Lambda_T H_{(i,j)}^n (S_{(i,j+1)}^n - S_{(i,j-1)}^n)}{2P_{(i,j)}^n \Delta\theta} - \Lambda_T P_{(i,j)}^n \frac{(H_{(i,j+1)}^n - H_{(i,j-1)}^n)}{2\Delta\theta} - \frac{\Lambda_T H_{(i,j)}^n S_{(i,j)}^n}{P_{(i,j)}^n \Delta\tau} - 2\Lambda_T P_{(i,j)}^n \frac{(H_{(i,j+1)}^{n+1} - H_{(i,j-1)}^n)}{\Delta\tau} \tag{31}$$

$$E_{(i,j)} S_{(i,j-1)}^{n+2} + F_{(i,j)} S_{(i,j)}^{n+2} + G_{(i,j)} S_{(i,j+1)}^{n+2} = I_{(i,j)} \tag{32}$$

$$E_{(i,j)} = -\frac{(H_{(i,j)}^{n+1})^3}{(\Delta\theta)^2} - \frac{\Lambda_T H_{(i,j)}^{n+1}}{4P_{(i,j)}^{n+1} \Delta\theta} + 3(H_{(i,j)}^{n+1})^2 \frac{H_{(i,j+1)}^{n+1} - H_{(i,j-1)}^{n+1}}{(2\Delta\theta)^2} \tag{33}$$

$$F_{(i,j)} = \frac{2(H_{(i,j)}^{n+1})^3}{(\Delta\theta)^2} + \frac{\Lambda_T H_{(i,j)}^{n+1}}{P_{(i,j)}^{n+1} \Delta\tau} \tag{34}$$

$$G_{(i,j)} = -\frac{(H_{(i,j)}^{n+1})^3}{(\Delta\theta)^2} + \frac{\Lambda_T H_{(i,j)}^{n+1}}{4P_{(i,j)}^{n+1} \Delta\theta} - \frac{R_r (H_{(i,j)}^{n+1})^3}{2\Delta\theta} - 3(H_{(i,j)}^{n+1})^2 \frac{H_{(i,j+1)}^{n+1} - H_{(i,j-1)}^{n+1}}{(2\Delta\theta)^2} \tag{35}$$

$$I_{(i,j)} = Q\delta_k + 3R_r^2 (H_{(i,j)}^{n+1})^2 \frac{(H_{(i,j+1)}^{n+1} - H_{(i,j-1)}^{n+1})(S_{(i,j+1)}^{n+1} - S_{(i,j-1)}^{n+1})}{(2\Delta R_r)^2} + R_r^2 (H_{(i,j)}^{n+1})^3 \frac{(S_{(i+1,j)}^{n+1} - 2S_{(i,j)}^{n+1} + S_{(i-1,j)}^{n+1})}{(\Delta R_r)^2} - \Lambda_T P_{(i,j)}^{n+1} \frac{H_{(i,j+1)}^{n+1} - H_{(i,j-1)}^{n+1}}{2\Delta\theta} - 2\Lambda_T P_{(i,j)}^{n+1} \frac{H_{(i,j)}^{n+2} - H_{(i,j)}^{n+1}}{\Delta\tau} + \frac{\Lambda_T H_{(i,j)}^{n+1} S_{(i,j)}^{n+1}}{P_{(i,j)}^{n+1} \Delta\tau} \tag{36}$$

By solving the Equation (27) and (32) using Thomas method, the pressure distribution of the thrust bearing can be obtained. The air film force (i.e., the restoring force of the thrust bearing) of the thrust bearing in z direction is given by

$$f_{btz} = P_s L_t^2 \int_0^{\frac{R_b - R_a}{L_t}} \int_0^{2\pi} P(R_r, \theta, \tau) \cos(\beta) R_r d\theta dR_r \tag{37}$$

And the torque of the air film force (i.e., the restoring torque of the thrust bearing) of the thrust bearing respect to the x axis and y axis is given by

$$t_{btx} = P_s L_t^2 \left(R_a + \frac{i(R_b - R_a)}{M_r} \right) \int_0^{\frac{R_b - R_a}{L_t}} \int_0^{2\pi} P(R_r, \theta, \tau) \cos(\beta) \sin(\alpha_{(i)}) R_r d\theta dR_r \quad (38)$$

$$t_{bty} = P_s L_t^2 \left(R_a + \frac{i(R_b - R_a)}{M_r} \right) \int_0^{\frac{R_b - R_a}{L_t}} \int_0^{2\pi} P(R_r, \theta, \tau) \cos(\beta) \cos(\alpha_{(i)}) R_r d\theta dR_r \quad (39)$$

2.3. Modeling of PMSM

Ideally, the magnetic force of PMSM is symmetric. However, the UMF will come out when the rotor eccentricity happens or the structure of the PMSM is not symmetric. Kawase et al. [31] used 3-D finite element method to analyze the UMF of the PMSM, and it is found that the axial component of the UMF is relatively small compared to other two components. Here, we assume the structure of the PMSM is symmetric and the axial component of the UMF is negligible. According to Maxwell stress tensor method, the 2D magnetic forces in the radial and tangential direction can be expressed as follows [32].

$$f_r = \int_0^{2\pi} \frac{1}{2\mu_0} (B_r^2 - B_\theta^2) r d\theta \quad (40)$$

$$f_\theta = \int_0^{2\pi} \frac{B_r B_\theta}{\mu_0} r d\theta \quad (41)$$

where B_r is the radial flux density, B_θ is the tangential flux density, μ_0 is the permeability of the air.

Figure 6 shows the schematic structure of motor with eccentric rotor [4], and the 2-D magnetic force in cartesian coordinates can be expressed as

$$f_{mx(i)} = f_{r(i)} \cos(\alpha_{(i)}) + f_{\theta(i)} \sin(\alpha_{(i)}) \quad (42)$$

$$f_{my(i)} = f_{r(i)} \sin(\alpha_{(i)}) + f_{\theta(i)} \cos(\alpha_{(i)}) \quad (43)$$

To simulate the 3-D state of the PMSM, the multiple slice method is employed. As shown in Figure 7, the magnetic force of the 3-D PMSM can be expressed as

$$f_{mx} = \sum_{i=i_0}^{i=i_m} f_{mx(i)} \quad (44)$$

$$f_{my} = \sum_{i=i_0}^{i=i_m} f_{my(i)} \quad (45)$$

And the magnetic torque of the 3-D PMSM is given by

$$t_{mx} = \sum_{i=i_0}^{i=i_m} f_{my(i)} \frac{i - i_b}{M_s} L_s \quad (46)$$

$$t_{my} = \sum_{i=i_0}^{i=i_m} f_{mx(i)} \frac{i - i_b}{M_s} L_s \quad (47)$$

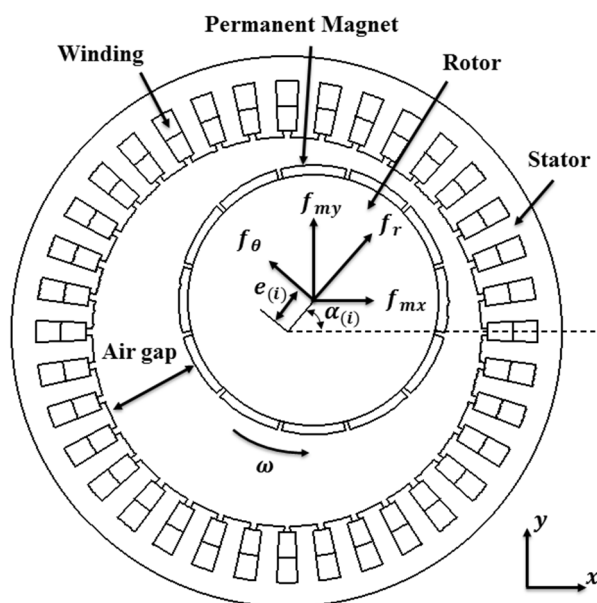


Figure 6. Schematic structure of the motor [4].

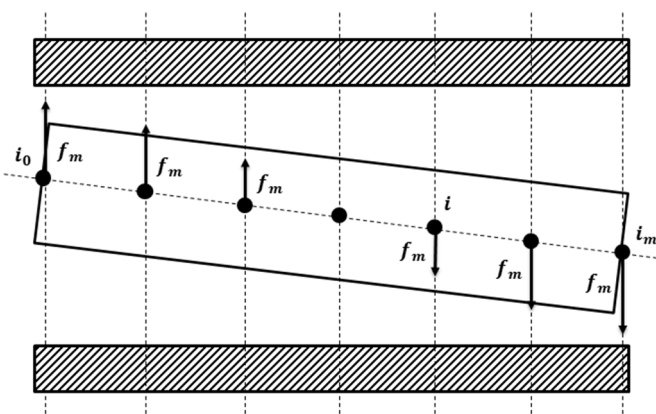


Figure 7. The simplified PMSM model using multiple slice method.

2.4. Dynamics Modeling of ABMS

The spindle shaft is regarded as a rigid rotor in the model, and the spindle shaft is considered to move with 5-DOF. The dimensionless acceleration, velocity and the attitude in the space can be calculated by

$$\{\ddot{\delta}\} = \frac{d^2\{\delta\}}{d\tau^2} = \{A\} \tag{48}$$

$$\{\dot{\delta}\} = \{\dot{\delta}_0\} + \{\ddot{\delta}\}\Delta\tau \tag{49}$$

$$\{\delta\} = \{\delta_0\} + \{\dot{\delta}\}\Delta\tau + \frac{1}{2}\{\ddot{\delta}\}(\Delta\tau)^2 \tag{50}$$

$$\{A\} = \left\{ \begin{array}{l} \frac{F_{eX} - F_{bX} + F_{mX}}{M} \\ \frac{F_{eY} - F_{bY} + F_{mY}}{M} \\ \frac{F_{eZ} - F_{bZ} + F_{mZ}}{M} \\ \frac{T_{eX} - T_{bX} + T_{mX} + (I_z - I_x)\dot{\Theta}_Y\dot{\Theta}_Z}{I_x} \\ \frac{T_{eY} - T_{bY} + T_{mY} + (I_y - I_z)\dot{\Theta}_Z\dot{\Theta}_X}{I_y} \end{array} \right\} \tag{51}$$

$$\{\delta\} = \begin{pmatrix} X \\ Y \\ Z \\ \Theta_X \\ \Theta_Y \end{pmatrix} \tag{52}$$

where the dimensionless parameters are given as follows.

$$\begin{aligned} X &= \frac{x}{C_r}, Y = \frac{y}{C_r}, Z = \frac{z}{C_r}, F_{ex} = \frac{f_{ex}}{P_s L_r^2}, F_{ey} = \frac{f_{ey}}{P_s L_r^2}, F_{ez} = \frac{f_{ez}}{P_s L_r^2}, F_{bx} = \frac{f_{bx}}{P_s L_r^2}, \\ F_{by} &= \frac{f_{by}}{P_s L_r^2}, F_{bz} = \frac{f_{bz}}{P_s L_r^2}, F_{mx} = \frac{f_{mx}}{P_s L_r^2}, F_{my} = \frac{f_{my}}{P_s L_r^2}, T_{ex} = \frac{t_{ex}}{P_s L_r^2 L_s}, T_{ey} = \frac{t_{ey}}{P_s L_r^2 L_s}, \\ T_{bx} &= \frac{t_{bjx} + t_{btx}}{P_s L_r^2 L_s}, T_{by} = \frac{t_{bjy} + t_{bty}}{P_s L_r^2 L_s}, T_{mx} = \frac{t_{mx}}{P_s L_r^2 L_s}, T_{my} = \frac{t_{my}}{P_s L_r^2 L_s}, \\ M &= \frac{m C_r \omega^2}{P_s L_r^2}, I_x = \frac{i_x \omega^2}{P_s L_r^2 L_s}, I_y = \frac{i_y \omega^2}{P_s L_r^2 L_s}, I_z = \frac{i_z \omega^2}{P_s L_r^2 L_s} \end{aligned}$$

where F_{ex}, F_{ey}, F_{ez} are the dimensionless external force applied on the spindle shaft in x, y, z direction, F_{bx}, F_{by}, F_{bz} are the dimensionless air film force in x, y, z direction, F_{mx}, F_{my} are the dimensionless UMF in x, y direction, T_{ex}, T_{ey} are the dimensionless external torque with respect to x, y axis, T_{bx}, T_{by} are the dimensionless air film torque with respect to x, y axis, T_{mx}, T_{my} are the dimensionless magnetic torque with respect to x, y axis, M is the dimensionless mass of the spindle shaft, I_x, I_y, I_z are the rotational inertia of the spindle shaft with respect to x, y, z axis, X, Y, Z are the dimensionless displacement in x, y, z direction, Θ_X, Θ_Y are the rotation angle of the spindle shaft with respect to x, y axis.

The spindle shaft is still at the initial condition, thus $\{\delta\} = \{0\}$ at the initial time. The flow chat for calculating the 5-DOF dynamics model of the ABMS is shown in Figure 8.

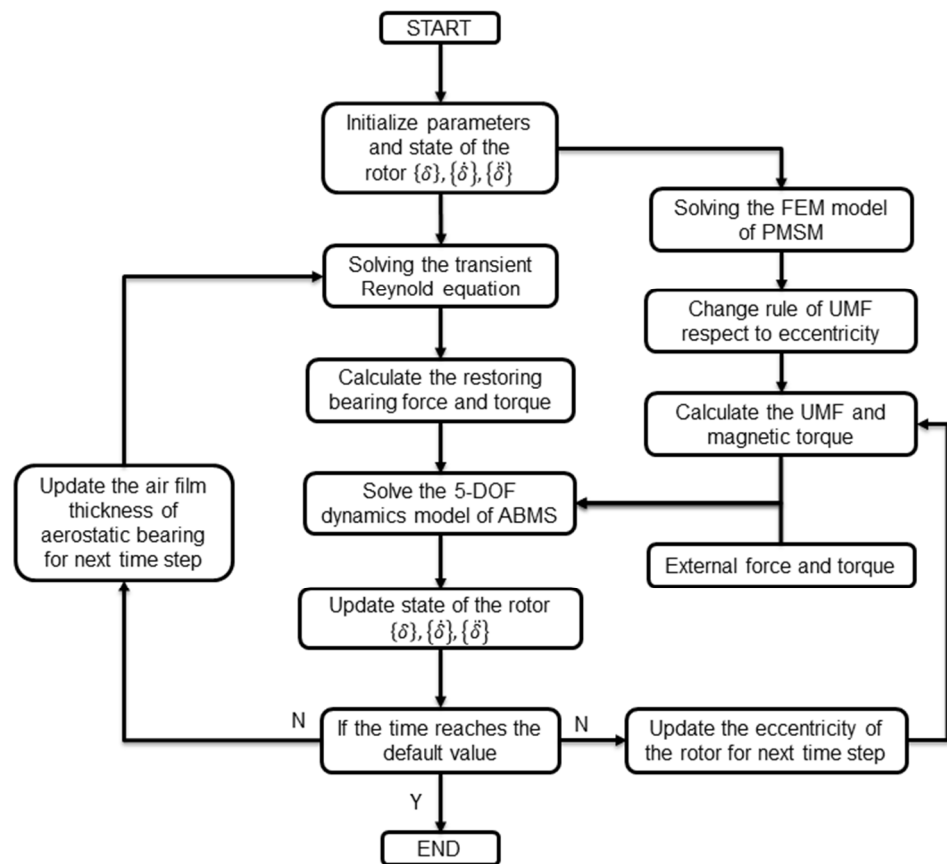


Figure 8. Flow chat for calculating the 5-DOF dynamics model of ABMS.

3. Numerical Simulation

3.1. Detailed Parameter

A case study is conducted to verify the effectiveness of the dynamics model of the ABMS. Table 1 lists the detailed parameters of the simulated model.

Table 1. The parameter of simulated ABMS.

Parameter (Unit)	Data
Length of shaft (m)	0.4
Diameter of journal bearing (m)	0.1
Length of journal bearing (m)	0.1
Inner diameter of thrust bearing (m)	0.1
Outer diameter of thrust bearing (m)	0.18
Bearing clearance (m)	1×10^{-5}
Diameter of orifice (m)	0.0002
Row number of Orifice on journal bearing	2
Row number of Orifice on thrust bearing	1
Orifice number of each row	8
Ambient pressure (Pa)	101325
Supply pressure (Pa)	405300
Density of air (kg/m^3)	1.204
Kinetic viscosity of air ($\text{Pa}\cdot\text{s}$)	1.82×10^{-5}
Specific heat ratio of air	1.401
Flow coefficient	0.8
Outer Rotor diameter (m)	0.1
Outer stator diameter (m)	0.15
Inner rotor diameter (m)	0.106
Number of slots	36
Number of poles	12
Motor effective length (m)	0.08
Rotational speed (r/min)	3000
Winding form of motor	Three-phase of double layer winding
External force (N)	50 400

3.2. Numerical Result

The model selects the same motor parameter as that in reference [4], and the variation trend of UMF has been given as follows.

$$f_{mx} = \begin{cases} [(-4.4\varepsilon^2 + 7.4\varepsilon + 0.3) \cdot \sin(\frac{2\pi\omega}{60}t) + (9.4\varepsilon^2 - 3.1\varepsilon + 3.8)] \cdot \sin\theta_r & (\varepsilon \leq 0.5) \\ [(-4.4\varepsilon^2 + 7.4\varepsilon + 0.3) \cdot \sin(\frac{2\pi\omega}{60}t) + (7.0\varepsilon + 1.1)] \cdot \sin\theta_r & (\varepsilon > 0.5) \end{cases} \quad (53)$$

$$f_{my} = \begin{cases} [(-4.4\varepsilon^2 + 7.4\varepsilon + 0.3) \cdot \sin(\frac{2\pi\omega}{60}t) + (9.4\varepsilon^2 - 3.1\varepsilon + 3.8)] \cdot \cos\theta_r & (\varepsilon \leq 0.5) \\ [(-4.4\varepsilon^2 + 7.4\varepsilon + 0.3) \cdot \sin(\frac{2\pi\omega}{60}t) + (7.0\varepsilon + 1.1)] \cdot \cos\theta_r & (\varepsilon > 0.5) \end{cases} \quad (54)$$

$$\theta_r = \left(9.3\varepsilon^3 - 13.4\varepsilon^2 + 1.8\varepsilon + 2.8\right) \cdot \sin\left(\frac{2\pi\omega}{60}t\right) \quad (55)$$

Two cases are calculated, i.e., the dynamics model with 400 N and 50 N external force. In the first case, 400 N external force is applied on the shaft end in x direction, the default dimensionless time is set to be 100. Figure 9a shows the air pressure distribution of the aerostatic journal bearing, Figure 9b and c show the air pressure distribution of the front and rear aerostatic journal bearing respectively, And Figure 9d shows the integrated air pressure distribution vision of aerostatic bearing with 400 N external force at dimensionless time 100.

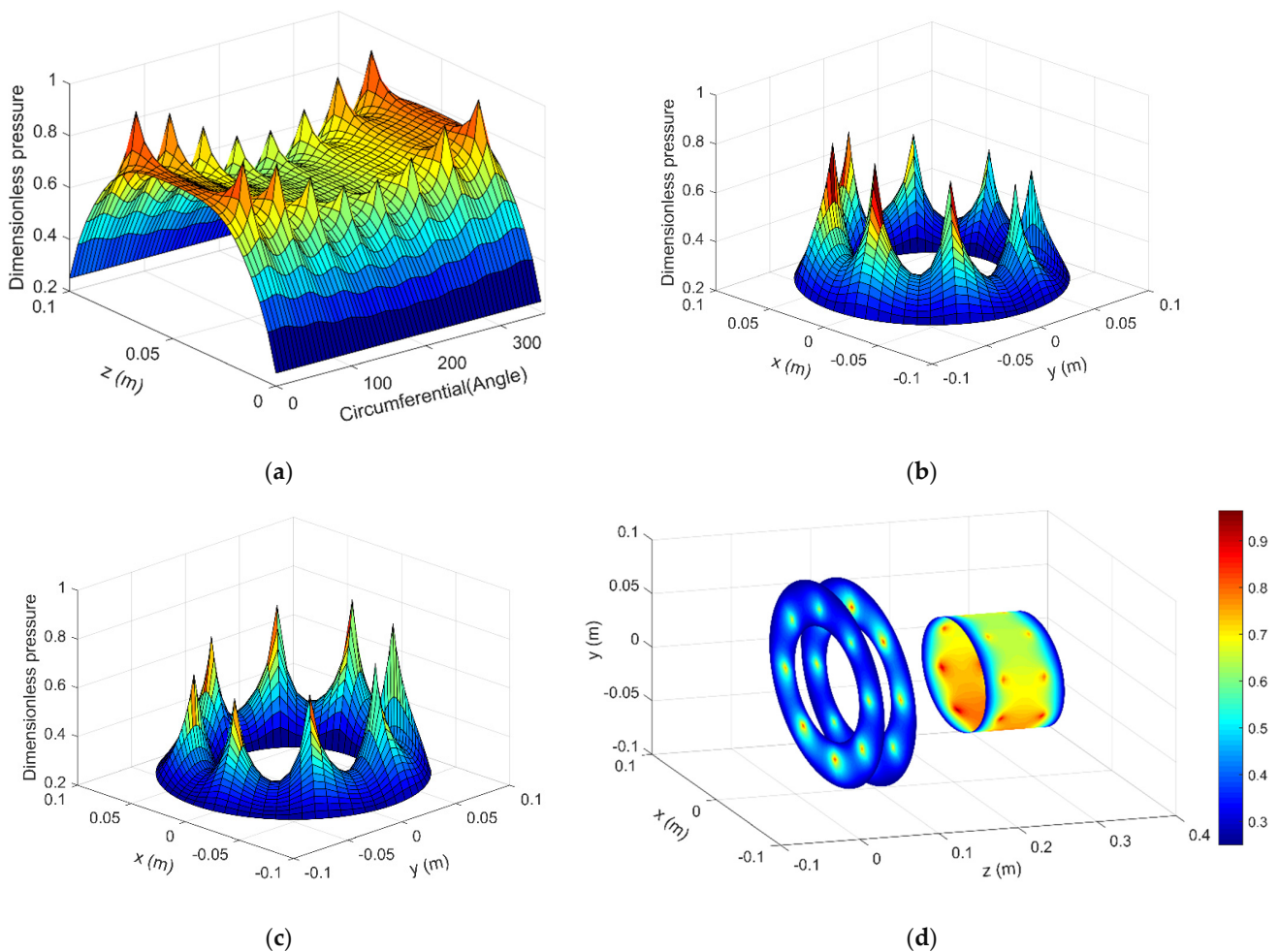


Figure 9. Pressure distribution of the aerostatic bearings with 400 N external force: (a) Journal bearing (b) Front thrust bearing (c) Rear thrust bearing (d) Integrated vision.

The result shows that when applies the external load on the shaft end, the spindle shaft can have a certain tilt angle and it affects the air pressure distribution of the aerostatic bearings obviously, which means the restoring force and torque of the air film applied on the spindle shaft are also changed. The tilt angle of the spindle shaft versus x axis and y axis is shown in Figure 10a,b, the tilt angle is converged and varies periodically with a certain amplitude, the extent of the tilt angle versus y axis is larger than the tilt angle versus x axis, this is mainly because the external force is applied in the x direction, thus the external torque is applied on y axis.

Figure 11a,b shows the motion trajectory of the shaft barycenter and the shaft end respectively. The result shows that the shaft acts stable with 400 N external force, its trajectory in x-y plane converged to a certain region. From a spatial perspective, the shaft end has left its initial position towards its balance position as shown in Figure 11c, and the displacement of the shaft end in z direction is shown in Figure 11d. The displacement in z direction is also converged and it varies periodically versus time.

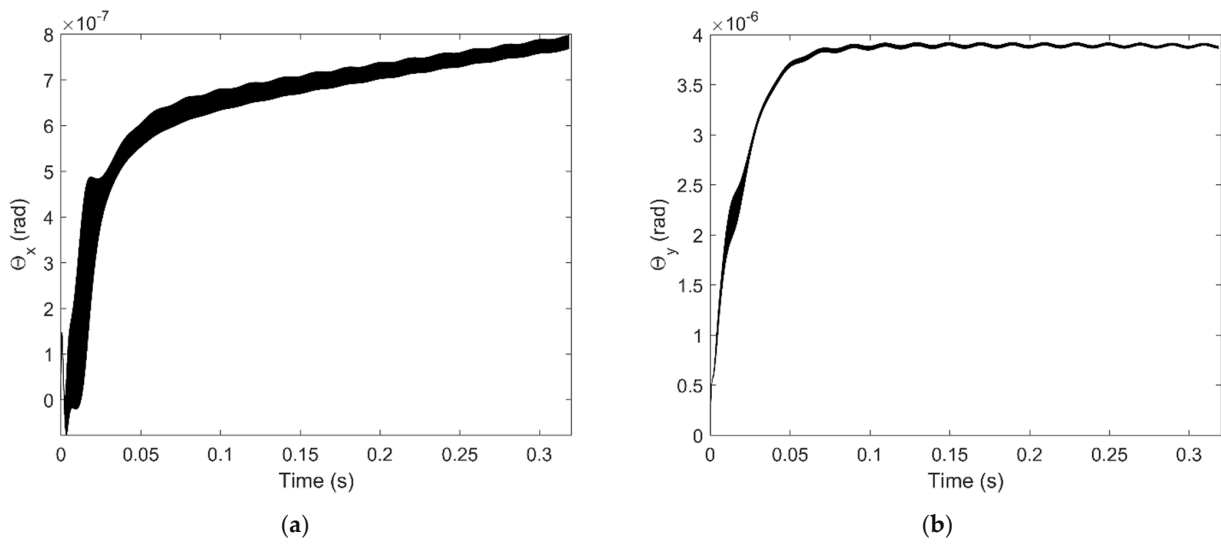


Figure 10. Tilt angle of the spindle shaft with 400 N external force: (a) Tilt angle versus x-axis (b) Tilt angle versus y-axis.

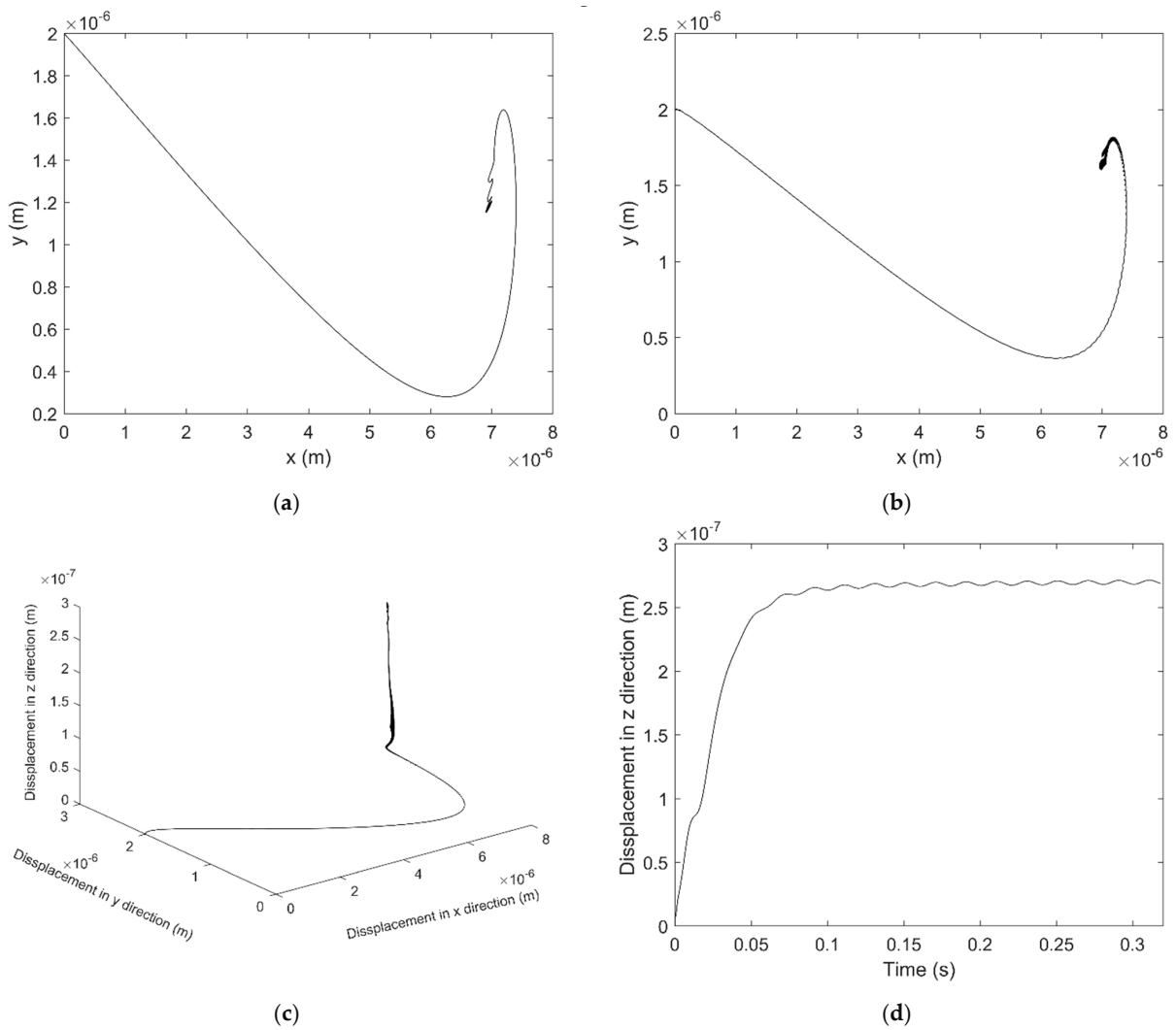


Figure 11. Motion trajectory of shaft with 400 N external force: (a) Position at the shaft barycenter in x-y plane (b) Position at the shaft end in x-y plane (c) Position at the shaft end in x-y-z coordinate (d) Position at the shaft end in z direction.

In the second case, 50 N external force is applied on the shaft end in x direction. The result is quite different with the first case, Figure 12a,b shows the tilt angle of the shaft versus x axis and y axis which are both diverged, which means the shaft is unstable under the current condition.

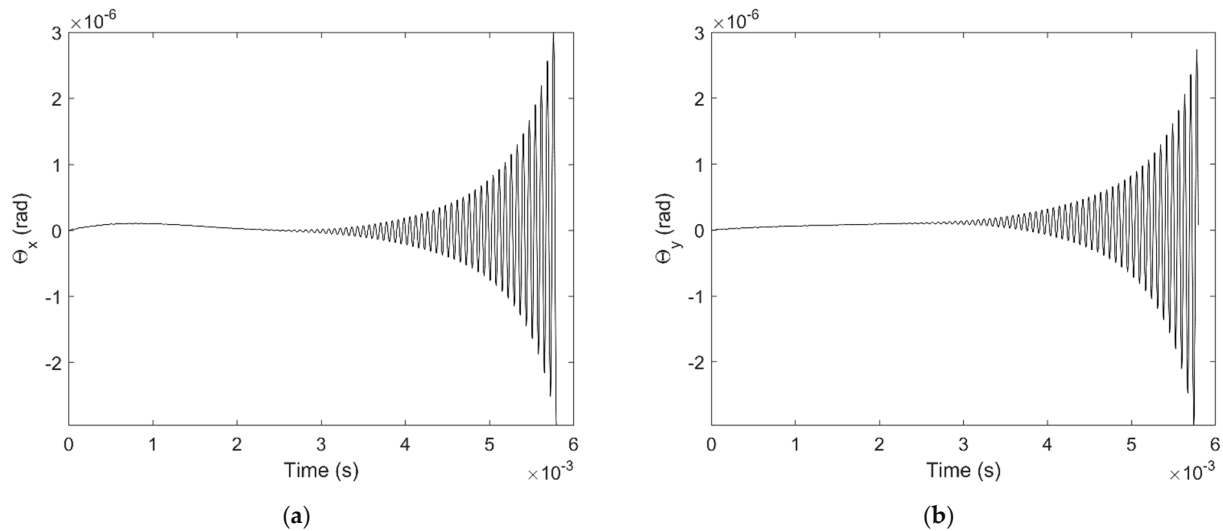


Figure 12. Tilt angle of the shaft with 50N external force: (a) Tilt angle versus x-axis (b) Tilt angle versus y-axis.

Figure 13a shows the corresponding air pressure distribution of the aerostatic journal bearing, Figure 13b,c show the air pressure distribution of the front and rear aerostatic journal bearing respectively, Figure 13d shows the integrated air film pressure distribution vision of aero-static bearing with 50 N external force at dimensionless time 100. According to the result, the air film pressure distribution of the aerostatic bearing becomes quite uneven, both the aerostatic journal bearing and the aerostatic thrust bearing show severe aerodynamic effect.

Figure 14a,b shows the motion trajectory of the shaft barycenter and the shaft end respectively. The result shows that the trajectory of shaft barycenter does not show the divergent trend while the trajectory of shaft end does, which means that the spindle shaft is at conical unstable state. It can be observed clearer in a spatial perspective as shown in Figure 14c, the trajectory of the shaft end moves as a spiral path. The displacement of the shaft end in the axial direction is also divergent as shown in Figure 14d.

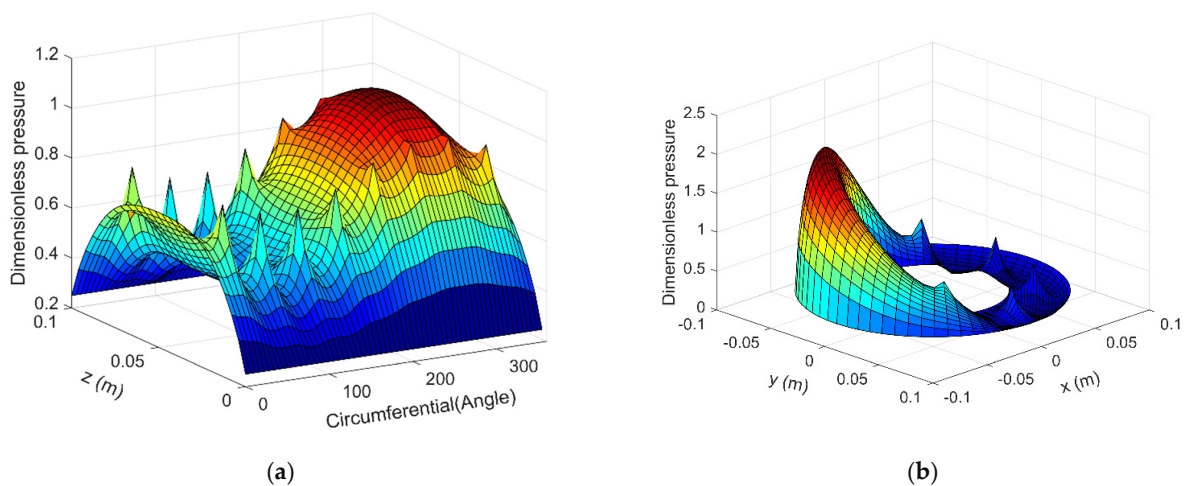


Figure 13. Cont.

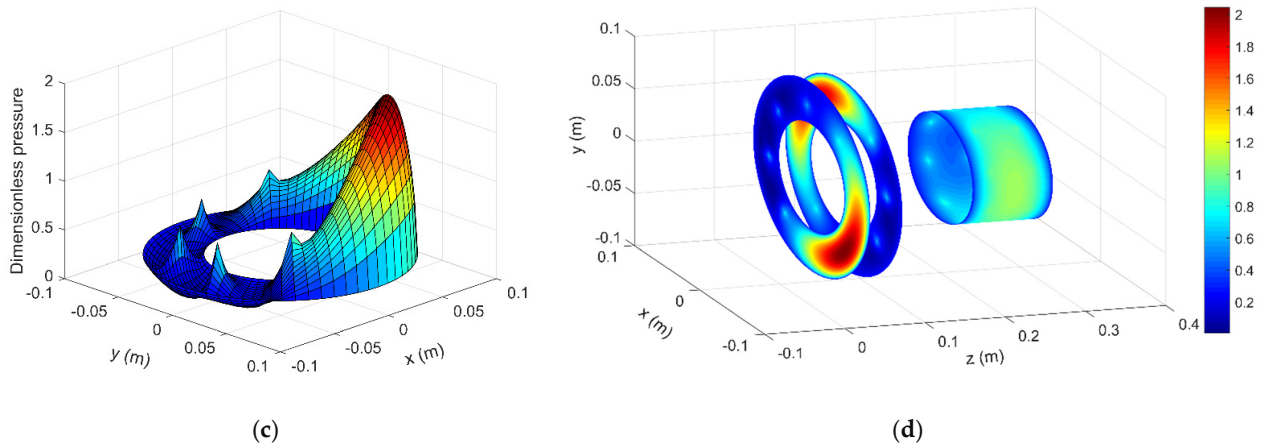


Figure 13. Pressure distribution of the aerostatic bearings with 50 N external force: (a) Journal bearing (b) Front thrust bearing (c) Rear thrust bearing (d) Integrated vision.

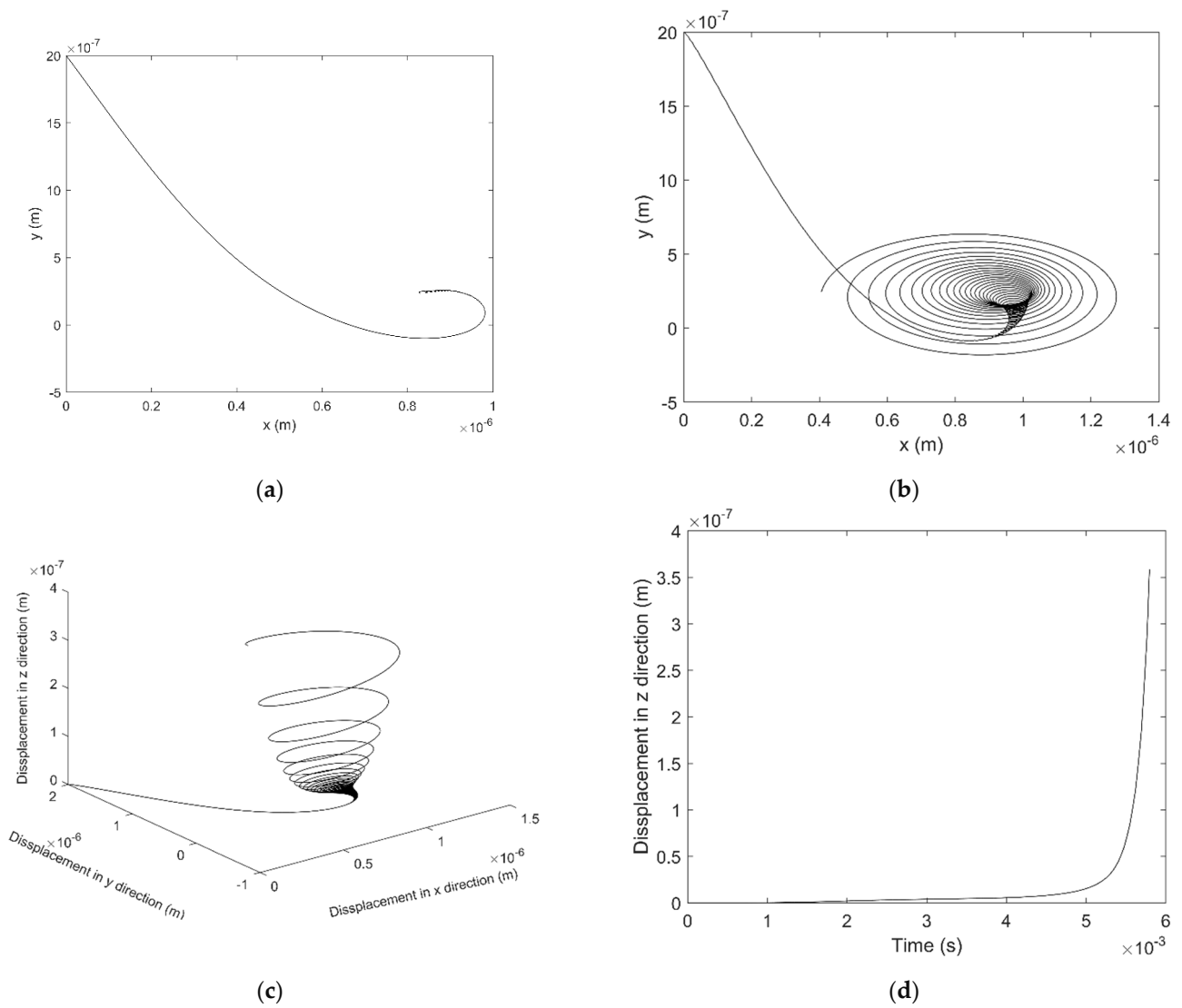


Figure 14. Motion trajectory of the aerostatic bearings with 50 N external force: (a) Journal bearing (b) Front thrust bearing (c) Rear thrust bearing (d) Integrated vision.

4. Discussion

In the motion process of the spindle shaft, the external force applied on the shaft end produce the torque on the shaft, resulting in the tilt motion of the shaft, then the distribution of the motor flux and the air film pressure is changed. Under the multi-field coupling effect of the external force, the air film force and the magnetic force, the shaft may finally stabilize in a certain spatial attitude or become unstable and even hit the bearing sleeve.

In this paper, a 5-DOF dynamics model of the aerostatic spindle was implemented using the restoring force method, while previous literatures mainly used the dynamic coefficient method [23,33]. The dynamic coefficient method improves the calculation speed compared to the restoring force method, but the dynamic behavior of the shaft can be obtained directly by employing the restoring force method. The proposed 5-DOF dynamic model of aerostatic spindle has considered the influence of the tilt motion and axial displacement of the shaft, which is neglected in the 2-DOF model. In the 2-DOF model of aerostatic spindle only the external force, the restoring force of the air film and the unbalanced magnetic force of the motor are considered, while the external torque, the restoring torque of the air film and the magnetic torque of the motor are not considered. However, they are all considered and integrated in the 5-DOF model. The motion trajectory of the shaft center in the 2D plane characterizes the dynamic behavior of the shaft, but it cannot show the conical motion of the shaft with the external force and external torque, which is quite important because the shaft has the spatial motion with 5-DOF.

In the simulation result, the dynamic behavior of the spindle shaft is stable with 400 N force and unstable with 50 N force. Similar phenomenon has been observed in the research of journal bearings, such as the research done by Khonsari et al. [34]. The stability boundary of the journal bearing varies with the change of the Sommerfeld Number, and the load on the bearing is one of the parameters that determine the value of the Sommerfeld Number. The stability boundary expands with the increase of the external load. To our knowledge, we think the reason behind dynamic behavior is probably the same as that of the journal bearings. That is, when the external load increase, the initial position locates in the unstable region under the low external load may locate in the stable region due to the expanding of the stability boundary. The Sommerfeld Number is also related to the rotation velocity [34]. Thus, the rotation velocity also affects the stability of the shaft, which is probably because that the change of the rotation velocity results in different aerodynamic effect and affects the stability. The critical value for distinguishing the stability of the shaft can be obtained in the 2-DOF model as the works done by Yang et al. [24]. It is sure that the critical value for the conical stability of the spindle shaft in the 5-DOF model also exists. It is meaningful to study the stability criterion of the shaft with 5-DOF. However, it will be much difficult to obtain the critical value in the 5-DOF model compared to that in the 2-DOF model. The 5-DOF model is much time costly to solve due to its high complexity and difficulty, thus, it will be further explored in the future research.

The proposed model can be improved in somehow. The shaft is regarded is a rigid body rather than the flexible body, and the structural deformation is neglected, however, it may have potential influence on the dynamic behavior of the shaft. Laha et al. [35] investigated the stability of the rotor supported by air journal bearing considering the rotor flexibility, in which the object was 2-DOF model. If the shaft is considered as a flexible rotor in a 5-DOF model, extra calculations need to be done, and the improvement of the solving code is also required. Due to the limitation of the current experimental condition, the validation of the theoretical results will be conducted in the future work.

5. Conclusions

In this study, a 5-DOF dynamics model of the aerostatic spindle is established. The modeling method and the numerical solution is given. Through the numerical model, the transient pressure distribution of the air film as well as the motion trajectory of the spindle shaft is obtained as expected. The result shows the significant meaning of considering the influence of the shaft tilt on the air film pressure distribution, which further determines the

restoring force and torque of the aerostatic bearing. Besides, the different conical stability behavior of the spindle shaft is shown under different external load through the model.

Author Contributions: Conceptualization, G.C.; methodology, G.C. and Y.C.; Software, Y.C.; data analysis, Y.C.; original draft writing, Y.C.; review and editing G.C. and Y.C.; supervision, G.C. All authors have read and agreed to the published version of the manuscript.

Funding: This work was supported by the National Natural Science Foundation of China (Grant No. 51705462), the Fundamental Research Funds for the Provincial Universities of Zhejiang (Grant No. RF-A2020005) and the Talent Project of Zhejiang Association for Science and Technology (Grant No. 2018YCCG016).

Informed Consent Statement: Not applicable.

Data Availability Statement: No new data were created or analyzed in this study. Data sharing is not applicable to this article.

Conflicts of Interest: The authors declare no conflict of interest.

References

- Chen, G.; Ju, B.; Fang, H.; Chen, Y.; Yu, N.; Wan, Y. Air bearing: Academic insights and trend analysis. *Int. J. Adv. Manuf. Technol.* **2019**, *106*, 1191–1202. [[CrossRef](#)]
- Chen, G.; Sun, Y.; Zhang, F.; An, C.; Chen, W.; Su, H. Influence of ultra-precision flycutting spindle error on surface frequency domain error formation. *Int. J. Adv. Manuf. Technol.* **2017**, *88*, 3233–3241. [[CrossRef](#)]
- Gao, Q.; Chen, W.; Lu, L.; Huo, D.; Cheng, K. Aerostatic bearings design and analysis with the application to precision engineering: State-of-the-art and future perspectives. *Tribol. Int.* **2019**, *135*, 1–17. [[CrossRef](#)]
- Chen, G.; Chen, Y.; Lu, Q.; Wu, Q.; Wang, M. Multi-physics fields based nonlinear dynamic behavior analysis of air bearing motorized spindle. *Micromachines* **2020**, *11*, 723. [[CrossRef](#)]
- Chen, Y.; Chiu, C.; Cheng, Y. Influences of operational conditions and geometric parameters on the stiffness of aerostatic journal bearings. *Precis. Eng. J. Int. Soc. Precis. Eng. Nanotechnol.* **2010**, *34*, 722–734. [[CrossRef](#)]
- Miyatake, M.; Yoshimoto, S. Numerical investigation of static and dynamic characteristics of aerostatic thrust bearings with small feed holes. *Tribol. Int.* **2010**, *43*, 1353–1359. [[CrossRef](#)]
- Yang, D.-W.; Chen, C.-H.; Kang, Y.; Hwang, R.-M.; Shyr, S.-S. Influence of orifices on stability of rotor-aerostatic bearing system. *Tribol. Int.* **2009**, *42*, 1206–1219. [[CrossRef](#)]
- Sun, Y.; Wu, Q.; Chen, W.; Luo, X.; Chen, G. Influence of unbalanced electromagnetic force and air supply pressure fluctuation in air bearing spindles on machining surface topography. *Int. J. Precis. Eng. Manuf.* **2021**, *22*, 1–12. [[CrossRef](#)]
- Zhang, S.; Yu, J.; To, S.; Xiong, Z. A theoretical and experimental study of spindle imbalance induced forced vibration and its effect on surface generation in diamond turning. *Int. J. Mach. Tools Manuf.* **2018**, *133*, 61–71. [[CrossRef](#)]
- Wu, Q.; Sun, Y.; Chen, W.; Chen, G.; Bai, Q.; Zhang, Q. Effect of motor rotor eccentricity on aerostatic spindle vibration in machining processes. *Proc. Inst. Mech. Eng. Part C J. Mech. Eng. Sci.* **2018**, *232*, 1331–1342. [[CrossRef](#)]
- Wu, Q.; Sun, Y.; Chen, W.; Wang, Q.; Chen, G. Theoretical prediction and experimental verification of the unbalanced magnetic force in air bearing motor spindles. *Proc. Inst. Mech. Eng. Part B J. Eng. Manuf.* **2019**, *233*, 2330–2344. [[CrossRef](#)]
- Zhang, J. Analysis on motion stability of a high-speed rotor-bearing system. *Chin. J. Mech. Eng.* **2005**, *18*, 220–223. [[CrossRef](#)]
- Wang, C.-C.; Lee, T.-E. Nonlinear dynamic analysis of bi-directional porous aero-thrust bearing systems. *Adv. Mech. Eng.* **2017**, *9*, 1–11. [[CrossRef](#)]
- Wang, C.-C. Application of a hybrid numerical method to the nonlinear dynamic analysis of a micro gas bearing system. *Nonlinear Dyn.* **2009**, *59*, 695–710. [[CrossRef](#)]
- Wang, C.-C. Theoretical and nonlinear behavior analysis of a flexible rotor supported by a relative short herringbone-grooved gas journal-bearing system. *Phys. D Nonlinear Phenom.* **2008**, *237*, 2282–2295. [[CrossRef](#)]
- Hei, D.; Lu, Y.; Zhang, Y.; Liu, F.; Zhou, C.; Müller, N. Nonlinear dynamic behaviors of rod fastening rotor-hydrodynamic journal bearing system. *Arch. Appl. Mech.* **2015**, *85*, 855–875. [[CrossRef](#)]
- Wang, C.-C. Application of a hybrid method to the nonlinear dynamic analysis of a flexible rotor supported by a spherical gas-lubricated bearing system. *Nonlinear Anal. Theory, Methods Appl.* **2009**, *70*, 2035–2053. [[CrossRef](#)]
- Zhang, G.-H.; Sun, Y.; Liu, Z.-S.; Zhang, M.; Yan, J.-J. Dynamic characteristics of self-acting gas bearing–flexible rotor coupling system based on the forecasting orbit method. *Nonlinear Dyn.* **2011**, *69*, 341–355. [[CrossRef](#)]
- Zhang, S.; To, S.; Wang, H. A theoretical and experimental investigation into five-DOF dynamic characteristics of an aerostatic bearing spindle in ultra-precision diamond turning. *Int. J. Mach. Tools Manuf.* **2013**, *71*, 1–10. [[CrossRef](#)]
- Li, J.; Liu, P. Dynamic analysis of 5-DOFs aerostatic spindles considering tilting motion with varying stiffness and damping of thrust bearings. *J. Mech. Sci. Technol.* **2019**, *33*, 5199–5207. [[CrossRef](#)]
- Li, J.; Huang, M.; Liu, P. Analysis and experimental verification of dynamic characteristics of air spindle considering varying stiffness and damping of radial bearings. *Int. J. Adv. Manuf. Technol.* **2019**, *104*, 2939–2950. [[CrossRef](#)]

22. Jiang, S.; Xu, C. Dynamics characteristics of a rotary table motorized spindle with externally pressurized air bearings. *J. Vibroengineering* **2017**, *19*, 801–811. [[CrossRef](#)]
23. Xu, C.; Jiang, S. Dynamic analysis of a motorized spindle with externally pressurized air bearings. *J. Vib. Acoust.* **2015**, *137*, 041001. [[CrossRef](#)]
24. Yang, P.; Zhu, K.-Q.; Wang, X.-L. On the non-linear stability of self-acting gas journal bearings. *Tribol. Int.* **2009**, *42*, 71–76. [[CrossRef](#)]
25. Wu, Y.; Feng, K.; Zhang, Y.; Liu, W.; Li, W. Nonlinear dynamic analysis of a rotor-bearing system with porous tilting pad bearing support. *Nonlinear Dyn.* **2018**, *94*, 1391–1408. [[CrossRef](#)]
26. Al-Bender, F. On the modelling of the dynamic characteristics of aerostatic bearing films: From stability analysis to active compensation. *Precis. Eng. J. Int. Soc. Precis. Eng. Nanotechnol.* **2009**, *33*, 117–126. [[CrossRef](#)]
27. Franssen, R.; Potze, W.; De Jong, P.; Fey, R.; Nijmeijer, H. Large amplitude dynamic behavior of thrust air bearings: Modeling and experiments. *Tribol. Int.* **2017**, *109*, 460–466. [[CrossRef](#)]
28. Lo, C.-Y.; Wang, C.-C.; Lee, Y.-H. Performance analysis of high-speed spindle aerostatic bearings. *Tribol. Int.* **2005**, *38*, 5–14. [[CrossRef](#)]
29. Powell, J.W. Theory of aerostatic lubrication. In *Design of Aerostatic Bearings*; The Machinery Publishing Co., Ltd.: Brighton, UK, 1970; pp. 35–66.
30. Rowe, W.B. Basic flow theory. In *Hydrostatic, Aerostatic and Hybrid Bearing Design*; Elsevier: Amsterdam, The Netherlands, 2012; pp. 25–48.
31. Kawase, Y.; Mimura, N.; Ida, K. 3-D electromagnetic force analysis of effects of off-center of rotor in interior permanent magnet synchronous motor. *IEEE Trans. Magn.* **2000**, *36*, 1858–1862. [[CrossRef](#)]
32. Meessen, K.K.; Paulides, J.J.; Lomonova, E.E. Force calculations in 3-D cylindrical structures using fourier analysis and the Maxwell Stress Tensor. *IEEE Trans. Magn.* **2012**, *49*, 536–545. [[CrossRef](#)]
33. Shi, J.; Cao, H.; Maroju, N.K.; Jin, X. Dynamic modeling of aerostatic spindle with shaft tilt deformation. *J. Manuf. Sci. Eng. Trans. ASME* **2019**, *142*, 1–43. [[CrossRef](#)]
34. Khonsari, M.M.; Chang, Y.J. Stability boundary of non-linear orbits within clearance circle of journal bearings. *J. Vib. Acoust.* **1993**, *115*, 303–307. [[CrossRef](#)]
35. Laha, S.K.; Banjare, H.; Kakoty, S.K. Stability analysis of a flexible rotor supported on finite hydrodynamic porous journal bearing using a non-linear transient method. *Proc. Inst. Mech. Eng. Part J J. Eng. Tribol.* **2008**, *222*, 963–973. [[CrossRef](#)]